A Role for the VPS Retromer in *Brucella* Intracellular Replication Revealed by Genomewide siRNA Screening

Alain Casanova,[a]* Shyan Huey Low,[a]* Maxime Québatte,[a] Jaroslaw Sedzicki,[a] Therese Tschon,[a] Maren Ketterer,[a] Kevin Smith,[a]* Mario Emmenlauer,[a]* Houchaima Ben-Tekaya,[a]* Christoph Dehio[a]

[a]Biozentrum, University of Basel, Basel, Switzerland

ABSTRACT *Brucella*, the agent causing brucellosis, is a major zoonotic pathogen with worldwide distribution. *Brucella* resides and replicates inside infected host cells in membrane-bound compartments called *Brucella*-containing vacuoles (BCVs). Following uptake, *Brucella* resides in endosomal BCVs (eBCVs) that gradually mature from early to late endosomal features. Through a poorly understood process that is key to the intracellular lifestyle of *Brucella,* the eBCV escapes fusion with lysosomes by transitioning to the replicative BCV (rBCV), a replicative niche directly connected to the endoplasmic reticulum (ER). Despite the notion that this complex intracellular lifestyle must depend on a multitude of host factors, a holistic view on which of these components control *Brucella* cell entry, trafficking, and replication is still missing. Here we used a systematic cell-based small interfering RNA (siRNA) knockdown screen in HeLa cells infected with *Brucella abortus* and identified 425 components of the human infectome for *Brucella* infection. These include multiple components of pathways involved in central processes such as the cell cycle, actin cytoskeleton dynamics, or vesicular trafficking. Using assays for pathogen entry, knockdown complementation, and colocalization at single-cell resolution, we identified the requirement of the VPS retromer for *Brucella* to escape the lysosomal degradative pathway and to establish its intracellular replicative niche. We thus validated the VPS retromer as a novel host factor critical for *Brucella* intracellular trafficking. Further, our genomewide data shed light on the interplay between central host processes and the biogenesis of the *Brucella* replicative niche.

IMPORTANCE With >300,000 new cases of human brucellosis annually, *Brucella* is regarded as one of the most important zoonotic bacterial pathogens worldwide. The agent causing brucellosis resides inside host cells within vacuoles termed *Brucella*-containing vacuoles (BCVs). Although a few host components required to escape the degradative lysosomal pathway and to establish the ER-derived replicative BCV (rBCV) have already been identified, the global understanding of this highly coordinated process is still partial, and many factors remain unknown. To gain deeper insight into these fundamental questions, we performed a genomewide RNA interference (RNAi) screen aiming at discovering novel host factors involved in the *Brucella* intracellular cycle. We identified 425 host proteins that contribute to *Brucella* cellular entry, intracellular trafficking, and replication. Together, this study sheds light on previously unknown host pathways required for the *Brucella* infection cycle and highlights the VPS retromer components as critical factors for the establishment of the *Brucella* intracellular replicative niche.

KEYWORDS *Brucella*, RAB7A, VPS retromer, VPS26, VPS35, replicative niche, siRNA

Cellular invasion is a common strategy shared by many bacterial pathogens of humans and animals in order to escape host defenses and to establish a protected replicative niche. Notably, this applies to the human pathogens of the genus *Salmo-*

nella, Shigella, Legionella, or Brucella (1–3). Knowledge of the host cellular pathways that are subverted by these pathogenic bacteria in order to reach and/or establish their intracellular replicative niches can be highly instructive for the development of new treatment strategies. Brucella is a facultative intracellular zoonotic pathogen causing animal and human brucellosis. With more than 300,000 new cases of human brucellosis every year, Brucella is regarded as one of the most important zoonotic bacterial pathogen worldwide (4–6). There is currently no effective vaccination for humans, and even prolonged combinatory antibiotic treatments do not fully protect against relapses (7). Therefore, Brucella remains a significant threat to public health and to the economy in areas of endemicity, and thus, new treatment strategies to circumvent Brucella infections are highly needed.

At the cellular level, Brucella invades both phagocytic and nonphagocytic cells where bacteria persist and replicate inside membrane-bound compartments—the Brucella-containing vacuoles (BCVs). BCVs sequentially interact with components of the host early and late endocytic pathway (endosomal BCVs [eBCVs]) and then transit to establish the replicative niche (replicative BCVs [rBCVs]) in vesicles that are directly connected to the endoplasmic reticulum (ER) (8) and harbor ER-specific markers, such as SEC61 and calnexin (8–10). Several critical steps for the intracellular journey of Brucella and their associated host factors have been resolved. For instance, adherence to the host cell surface is mediated via interaction with sialic acid residues or binding to fibronectin and vitronectin (11, 12). Internalization requires actin remodeling via the activity of the small GTPases RAC and RHO and direct activation of CDC42 (13). Upon internalization, bacteria are contained within eBCVs that successively associate with a subset of endosomal markers, starting with RAB5, the early endosomal antigen (EEA1), the transferrin receptor (TfR), as well as the lipid raft component flotillin-1 (9, 14–16). Next, the eBCVs associate with the late endosomal markers RAB7, RILP (RAB7's effector RAB-interacting lysosomal protein), and LAMP-1 (lysosome-associated membrane protein 1), and transiently with autophagosomal markers (9, 10). As they evolve late endosomal characteristics, acidification of the eBCVs serves as a trigger for the expression of the VirB type IV secretion system (T4SS) (17, 18). This major pathogenicity factor is required to prevent the complete fusion of eBCVs with lysosomes, consequently allowing a fraction of the internalized Brucella to avoid host-mediated degradation, and promotes the maturation of the eBCVs toward the rBCVs (16, 18). Noteworthy, the T4SS effectors responsible for this escape remain largely elusive, despite a growing repertoire of identified candidates (recently reviewed in reference 19). Most recently, it was discovered that subversion of both anterograde and retrograde transport and recruitment of conserved oligomeric Golgi (COG) tethering complex-dependent vesicles to the BCV promotes the establishment of the Brucella replicative niche (20). Importantly, despite all these findings, the precise mechanism(s) resulting in diversion of eBCVs from the endolysosomal pathway toward the ER-associated replicative compartment (rBCVs) is still largely unresolved. The same holds true for host factors required for maintenance of the replicative niche.

In this study, we took a systems-level approach to gain deeper insight into these fundamental questions. Using a genomewide RNA interference (RNAi) screening approach, we identified 425 host proteins whose knockdown either increases (202) or decreases (223) Brucella intracellular replication. Beside the rediscovery of several previously identified host targets, which validates our approach, data reveal numerous novel candidate components that can modulate Brucella cellular entry, trafficking, and/or replication. Among these targets, we identified VPS35 and VPS26A, two components of the trimeric vacuolar protein sorting (VPS) complex (termed VPS retromer here), which are required for the diversion of BCVs from the endolysosomal pathway and the establishment of the intracellular replicative niche.

RESULTS

A genomewide siRNA screen reveals novel host pathways involved in Brucella infection. To identify novel host factors important for Brucella intracellular infection, we
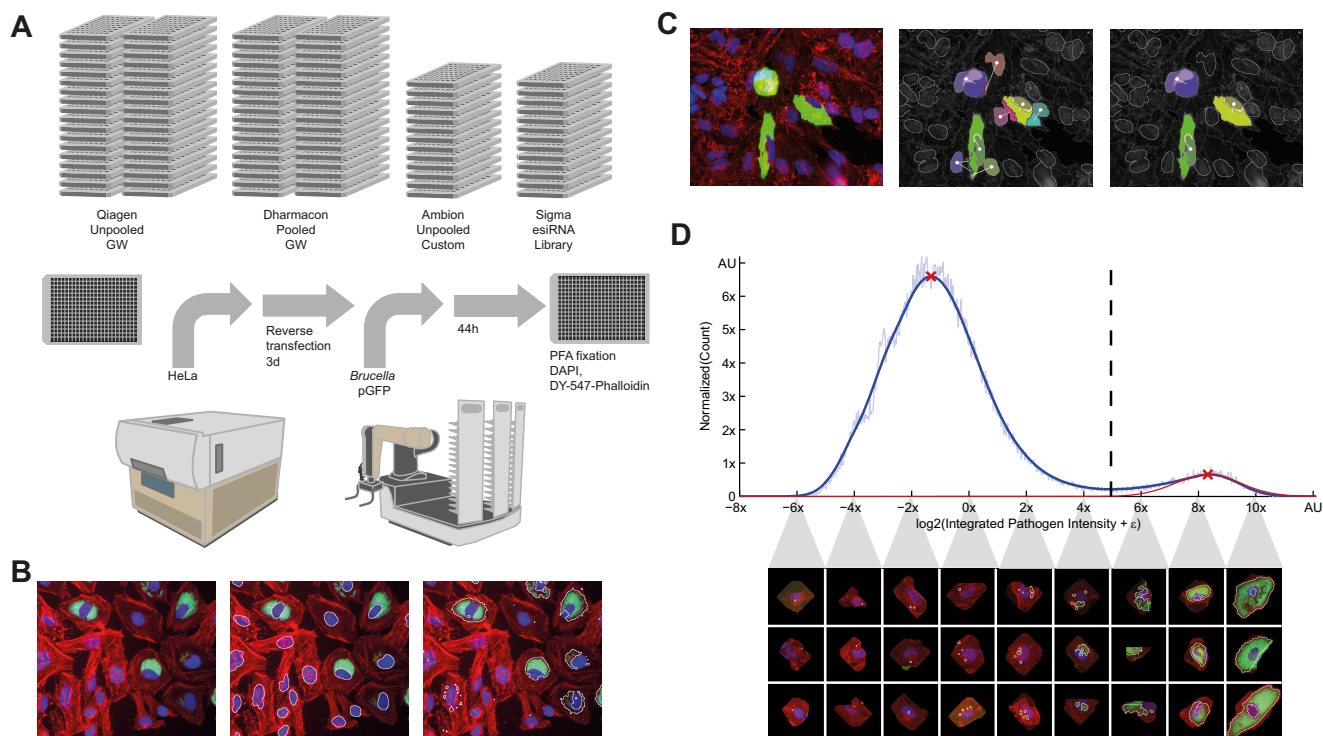
FIG 1 Overview of the high-content screening and analysis. (A) Summary of RNAi screening workflow. Reverse transfection of HeLa cells was performed in 384-well format for 72 h, followed by 48-h infection with GFP-expressing *B. abortus*, PFA fixation, and staining of HeLa cells with DAPI and DY-547−phalloidin before automated imaging. GW, genomewide. (B) Image analysis was performed with CellProfiler to segment nuclei and bacteria and to extract measurements. (C) Accurate association of segmented bacteria to nuclei enables quantitative single-cell measurements. The naive association (middle image) of segmented pathogen can be affected by oversplitting in dense cell populations (left image). Our proposed solution (right image) based on a nucleus attraction score. (D) The plate histogram shows the bimodal distribution of integrated GFP intensity corresponding to *Brucella* replication. Intensity on the *x* axes is $\log_2$ scaled to account for exponential growth. The normal distribution fitted (red curve) to the kernel density estimation of the histogram allows us to compute a robust binary infection threshold (dashed line) separating HeLa cells with (right) and without (left) replicating *Brucella*. Associated are samples of single-cell images corresponding to the intervals of the intensity distribution (for more details, see Materials and Methods).

performed a genomewide small interfering RNA (siRNA) perturbation screen on the human epithelial cell line HeLa (ATCC CCL-2) combined with bacterial infection at biosafety level 3. Infections of the siRNA-treated cells were performed with a green fluorescent protein (GFP)-expressing strain of *Brucella abortus*, and the outcome was analyzed at 48 h postinfection (hpi) using automated fluorescence microscopy (21, 22). Infection scoring was determined with a tailored high-content analysis workflow (Fig. 1 and Materials and Methods). In brief, a model of *Brucella* replication was fitted to the pathogen intensity distribution to gain an infection classification independent of absolute fluorescence intensity. Further, we implemented an image intensity normalization coupled with a novel pathogen-to-cell association approach, which enabled quantitative measurement of the pathogen intensity distribution (Materials and Methods). An overview of the results is presented in Fig. S1 in the supplemental material. To account for the well-known confounding off-target effects associated with siRNA technology (recently reviewed in reference 23), we applied a multiple orthologous RNAi reagent approach (MORR) (24) with $n \geq 5$ perturbations per host gene. Further, we applied the redundant siRNA analysis (RSA) algorithm (25) on the entire screening data to reduce the number of false-positive results caused by off-target effects of single siRNAs and to favor genes with a reproducible phenotype confirmed by independent siRNAs. Genes matching a Benjamini-corrected RSA *P* value of ≤0.01 with more than three hit wells were considered significant and selected for further analysis (see also Materials and Methods). As a result, we identified 425 significant hits affecting *Brucella* infection. These comprised 223 down-hits (Fig. S1A, red, and Table S1) and 202 up-hits (Fig. S1A, green, and Table S2). Single siRNA data points are presented in Fig. S2

(down-hits) and Fig. S3 (up-hits). A panel of representative images from the screen is presented in Fig. 2A. Hit genes were further stratified by gene annotation enrichment analysis and functional annotation clustering using DAVID (26), protein-protein interaction network using the STRING database (27), as well as manual data mining. The functional categories enriched in our hit lists are presented in Fig. 2B to D together with the high-confidence protein-protein interaction network for targets that reduced (Fig. 2E) or increased (Fig. 2F) *Brucella* infection upon knockdown. Gene ontology and functional clustering analysis indicated a rather small overlap in enriched pathways when considering up- or down-hits (Fig. 2B to D). The most prominent clusters that positively affected infection upon knockdown comprised components involved in the control or modulation of central cellular processes, such as protein synthesis, transcription, and mRNA processing, and cell cycle progression, as well as clathrin-mediated endocytosis (Fig. 2 and Table S2). The most prominent clusters that negatively affected infection upon knockdown comprised signaling pathways involved in actin remodeling and phagocytosis. These clusters included most core components of the actin-related protein-2/3 complex (ARP2/3) (ARPC2, ARPC3, ACTR2, and ACTR3), and one of its main modulator, the WASP regulatory complex (WRC) (CYFIP1, WASF3, NCKAP1, and ABI3). Down-hits also comprised multiple components involved in transforming growth factor beta (TGF-β) and erythropoietin-producing human hepatocellular receptors (Eph) signaling as well as further vesicular/endocytic pathways (Fig. 2 and Table S1). Among all these factors, we can highlight the Ras-related protein RAB7A, which is needed for *Brucella* trafficking to the replicative niche (10), the small GTPases RAC1 and CDC42, which are involved in *Brucella* internalization into nonphagocytic cells (13), as well as the transmembrane glycoprotein SLC3A2 (CD98hc), involved in both bacterial uptake and intracellular multiplication (28). Since the roles of these individual components have already been described in the context of *Brucella* infection, they can be considered benchmarks for our results and globally validate our systems-level perspective of the human infectome for *Brucella* infection.

Pathogen entry assay identifies a role for VPS35, VPS26A, and SEC61γ in *Brucella* postentry trafficking. To further dissect the roles of the identified genes in the progression of *Brucella* infection, we took advantage of a pathogen entry assay previously developed in our laboratory (29). Briefly, at 4 hpi, host cell membrane-impermeable gentamicin was added to selectively kill extracellular *Brucella*, and concomitantly, cell membrane-permeable anhydrotetracycline was added to induce expression of a plasmid-encoded reporter in the viable intracellular bacteria. At 8 hpi, this approach allowed us to robustly identify individual intracellular bacteria and to quantify the bacterial load before intracellular replication is initiated (Fig. 3A and Materials and Methods). For this assay, we selected a number of genes from the different pathways identified in the genomewide screen as well as additional genes supplementing them (Table S3). The results of this entry assay were plotted against a matching endpoint assay (intracellular replication at 48 hpi). Strikingly, most of the genes tested displayed a direct correlation between the results of the entry assay and the endpoint assay ($r^2 = 0.763$). This was the case for components involved in the actin-remodeling pathway (RAC1, ACTR3, and CYFIP1) or those involved in the TGFβ signaling (SMAD4, TGFBR1, and TGFBR2), which strongly reduced both entry and subsequent intracellular replication (Fig. 3B and Table S3). Similarly, the components of the clathrin pathway GAK and AP2S1 both increased bacterial entry and replication (Fig. 3B and Tables S3 and S4). This supports their involvement in *Brucella* entry into nonphagocytic cells, without excluding an additional role at any further stage of the infection. To identify components with a divergent outcome between the entry and replication assays, we selected genes diverging by more than 1 standard deviation to the fitted data. Six genes matched this criterion (Fig. 3B). Three genes displayed an apparent higher effect on pathogen entry than subsequent replication (albeit at a rather modest level). These were the small GTPases CDC42 (13), the α1 subunit of the Na$^+$, K$^+$-ATPase ATP1A1 (30) and the subtilisin-like endoproteinases FURIN (31). Most strikingly, three genes displayed a stronger reduction in endpoint replication compared to entry. Knockdown of
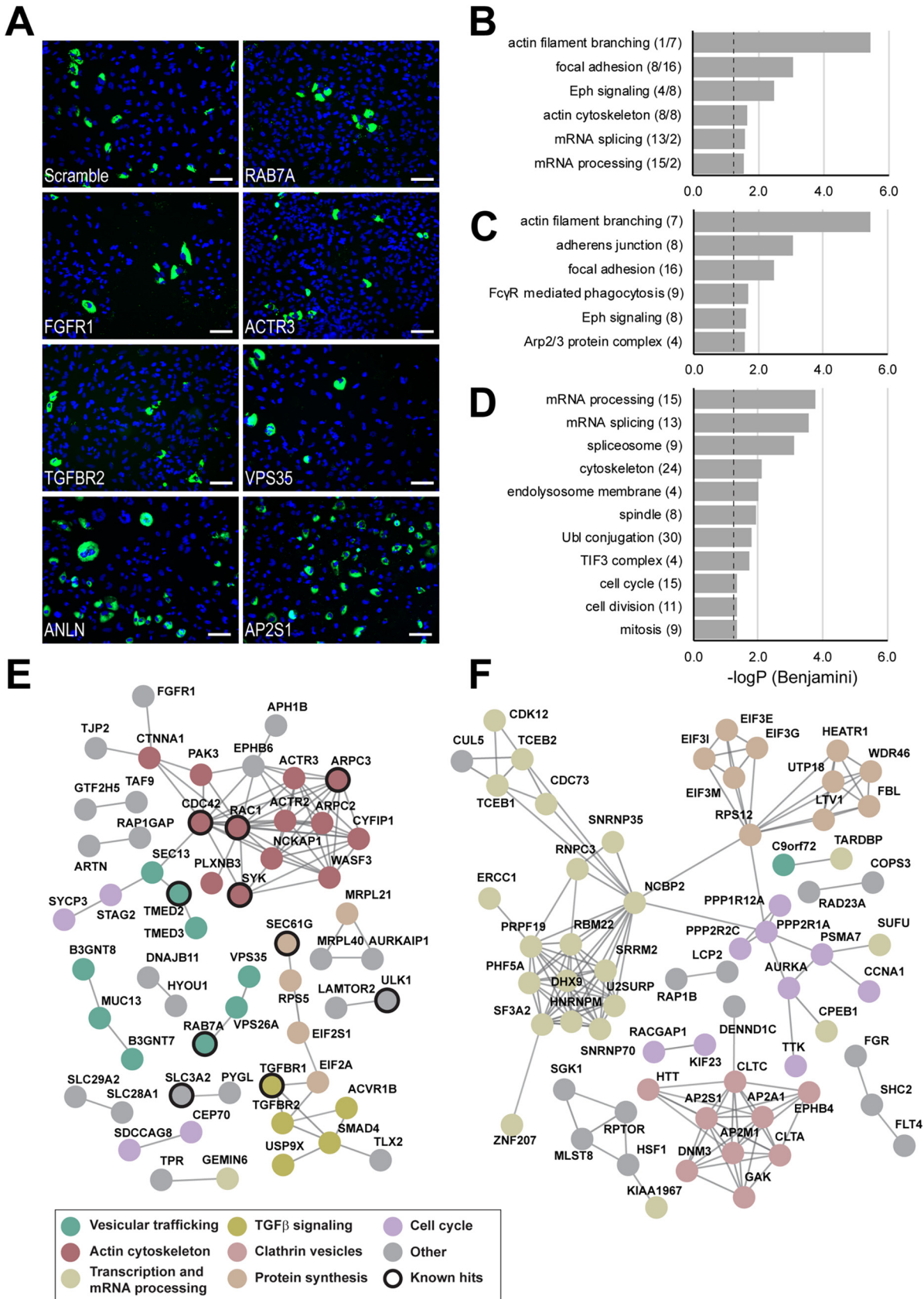
FIG 2 The human infectome for *Brucella* infection determined by genomewide siRNA screening. (A) Representative merged images from the genomewide screen showing nuclei (DAPI) and intracellular replication of GFP-expressing *Brucella abortus* for either control conditions
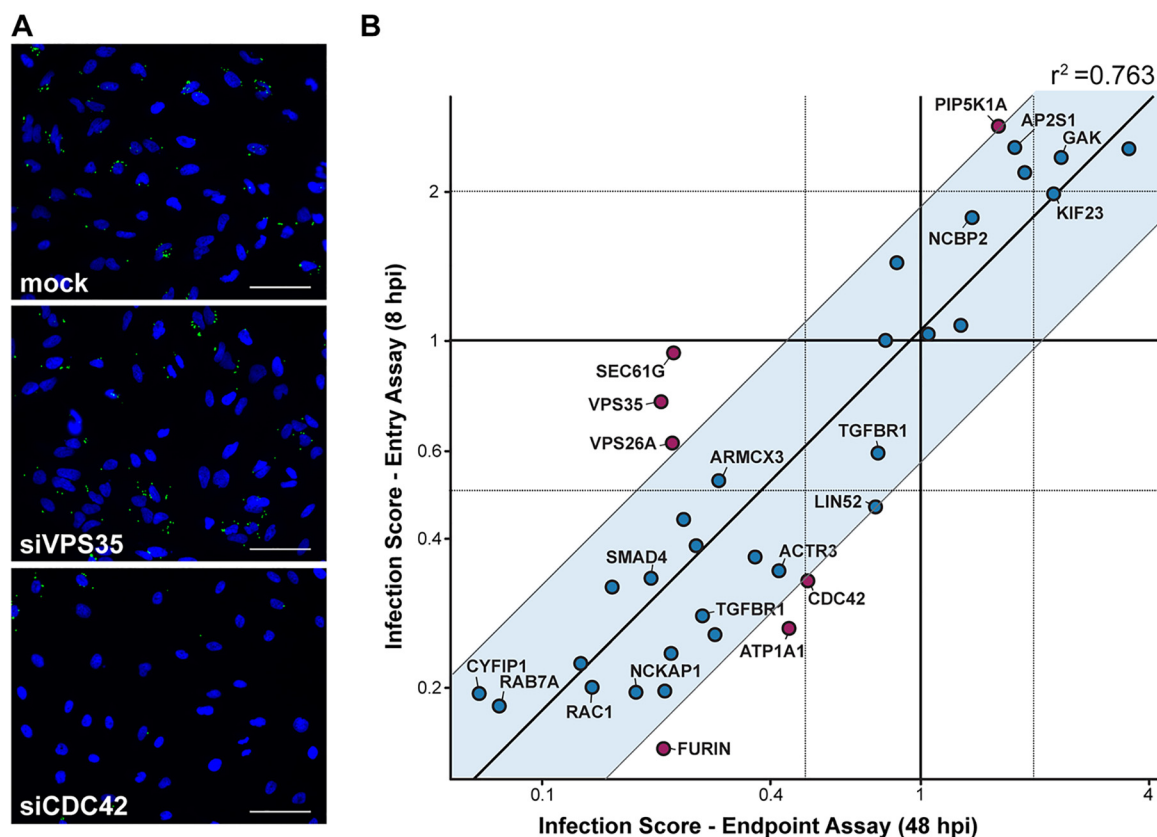
FIG 3 Entry assay identifies new components required for postentry processes during *Brucella* infection. (A) Representative images from the entry assay showing nuclei (DAPI) of HeLa cells and intracellular *Brucella abortus* (GFP) for control condition (mock) and cells treated with siRNAs against CDC42 or VPS35. HeLa cells were infected with *B. abortus* expressing GFP under a tetracycline-inducible system for 8 h (see Materials and Methods). Bars = 100 μm. (B) Scatter plot in double logarithmic scale showing infection scores measured for the entry assay (8 hpi) versus endpoint assay (48 hpi), normalized to the respective mock data set (Table S3). For the entry assay, cells containing single bacteria were considered infected, and the final readout is proportional to the median number of bacteria per infected cells. For the endpoint assay, only cells containing replicating bacteria were considered infected (Fig. 1 and Materials and Methods). Each data point corresponds to the average of all siRNAs or esiRNAs targeted against the gene of interest ($n = 3$). The straight fit (oblique line, $r^2 = 0.763$) indicates a globally high correlation between both assays. The blue region shows all points within 1 standard deviation (SD) of the fitted data. The genes falling out of this range are marked in red. For ease of visualization, only the averaged values over all RNAi products targeting a given gene are displayed.

Sec61γ, a central element of the ER-protein translocation machinery (see, for instance, reference 32), which has been previously involved in *Brucella* infection (33), showed a strong decrease in intracellular replication albeit no effect on pathogen entry. Similarly, our assay identified the vacuolar protein sorting-associated proteins VPS35 and VPS26A—two essential components of the VPS retromer complex (recently reviewed in references 34 and 35). These genes and associated pathway(s) thus likely represent novel components controlling the postentry trafficking of *Brucella* toward its replicative niche and/or are themselves required for the establishment or maintenance of the

FIG 2 Legend (Continued)

(scramble) or a panel of identified hits (RAB7A, FGFR1, ACTR3, TGFBR2, VPS35, ANLN, and AP2S1). Bars = 100 μm. (B to D) Results of gene ontology enrichment analysis (DAVID) for the entire hit list (B), the down-hits (C), or up-hits (D). The $-\log_{10}$ values of the P values associated with the different categories are indicated (cutoff, Benjamini corrected P value ≤ 0.01, with more than 3 hit wells) as well as the number of individual components associated with the displayed categories are indicated. In panel B, the first number is the number of down-hits and the second number is the number of up-hits. (E and F) High-confidence protein-protein interaction networks ($x \geq 0.8$) for the 223 RSA down-hits (A) or 202 up-hits (B) determined using the STRING database. Clusters with common predicted cellular function are colored, and their prominent functions are indicated. Hits previously reported to be involved in *Brucella* pathogenicity are highlighted: ARPC3 (29), TGFBR2 (22), SEC61G and TMED2 (33), RAC1 and CDC42 (13), SLC3A2 (28), RAB7A (10), SYK (63), and ULK1 (64). For clarity, disconnected components are not displayed. The complete lists of down- and up-hits are presented in Tables S1 and S2 in the supplemental material. Data from single RNAi reagents for down- and up-hits are presented in Fig. S2 and S3.

rBCVs. For the present study, we further focused on the roles of VPS35 and the VPS retromer in *Brucella* trafficking, as it was the most prominent hit in our entry assay.

The VPS retromer is important for *Brucella* intracellular replication. The retromer complex orchestrates the recycling of numerous transmembrane proteins from early and maturing endosomes either to the trans-Golgi network (TGN) or back to the plasma membrane. Formed by a heterotrimeric complex consisting of VPS26, VPS29, and VPS35, the VPS retromer is conserved from yeast to human. However, the individual retromer subcomplexes have functionally diverged to organize multiple distinct sorting pathways, depending on the association with different accessory factors (34, 35). To further decipher the role of the retromer in *Brucella* trafficking and intracellular replication we specifically browsed our genomewide siRNA data for retromer-associated proteins (Fig. 4A and D). In addition to VPS35 and VPS26A, already identified both in the genomewide screen and in the entry screen (Fig. 2E and Fig. 3B), knockdown of VPS26B (the paralogue of VPS26A) resulted in a significant reduction in *Brucella* infection (Fig. 4D). Depletion of VPS29, the third core component of the VPS retromer, resulted only in a mild reduction of *Brucella* infection and did not reach significance due to the wide spread of data obtained for the cohort of nine individual siRNAs tested (suggestive of strong off-target effects). Next to the retromer components, knockdown of the small GTPase RAB7A showed the strongest reduction in intracellular *Brucella* (Fig. 4D). However, neither SNX3, that together with the VPS retromer forms the SNX3 retromer, nor SNX27, another retromer-associated component involved in endosome-to-plasma membrane trafficking (36, 37), displayed significant effect (Fig. 4D). Depletion of SNX1 and SNX5, two of the four sorting nexins of the SNX-BAR retromer (38), even seems to enhance *Brucella* infection (although they did not pass our hit selection criterion), while the two others, SNX2 and SNX6, showed no effect (Fig. 4D). Noteworthy, the functional association of the SNX-BAR sorting nexins with the VPS retromer has been challenged by two recent publications, which rather support a VPS-independent action of SNX-BAR (39, 40). Collectively, our data indicate that the observed postentry impairment in *Brucella* intracellular replication is specifically linked to the integrity of the heterotrimeric VPS retromer, although involvement of further components in this process cannot be excluded.

To validate the requirement of VPS35 on *Brucella* infection and to rule out any off-target effects, we performed a complementation experiment using a VPS35 cDNA insensitive to a coexpressed shRNA (41). While shRNA knockdown of endogenous VPS35 inhibited *Brucella* infection, as detected in our genomewide approach, ectopic expression of the shRNA-insensitive cDNA of VPS35 rescued the phenotype (Fig. 4B and C), confirming that depletion of VPS35 indeed negatively affects *Brucella* infection. We further confirmed the observed requirement of the VPS retromer for *Brucella* intracellular replication by determining intracellular bacterial load at different infection times of siRNA-transfected cells using CFU determination (Materials and Methods). At 6 hpi, no significant difference to the control was detected, with the exception of a small increase in intracellular bacteria upon VPS35 knockdown (Fig. 4E). Importantly, at 20 h and 44 hpi, siRNA knockdown of either VPS35, VPS29, or VPS26 resulted in a significant decrease of viable intracellular *Brucella* compared to control-treated cells (Fig. 4E), confirming the data obtained by our microscopy-based entry screen (Fig. 3). Further, efficiency of siRNA knockdown was confirmed by Western blot analysis (Fig. 4F and Table S4). Together, these results corroborate the importance of each constituent of the VPS retromer, including VPS29, for *Brucella* to reach and possibly to maintain its intracellular replicative niche.

VPS35 knockdown prevents *Brucella* escape from the lysosomal pathway. Transient association with the lysosomal marker LAMP-1 is a hallmark of BCV trafficking during the first hours of infection. This association is eventually lost for those bacteria that manage to escape the host degradative pathway. Thus, to investigate the role of VPS35 in *Brucella* trafficking and to assess at which stage it could be required for the establishment of the intracellular replicative niche, we quantified *Brucella* colocalization with LAMP-1 in siRNA-treated and control cells. To this end, we analyzed *Brucella*-
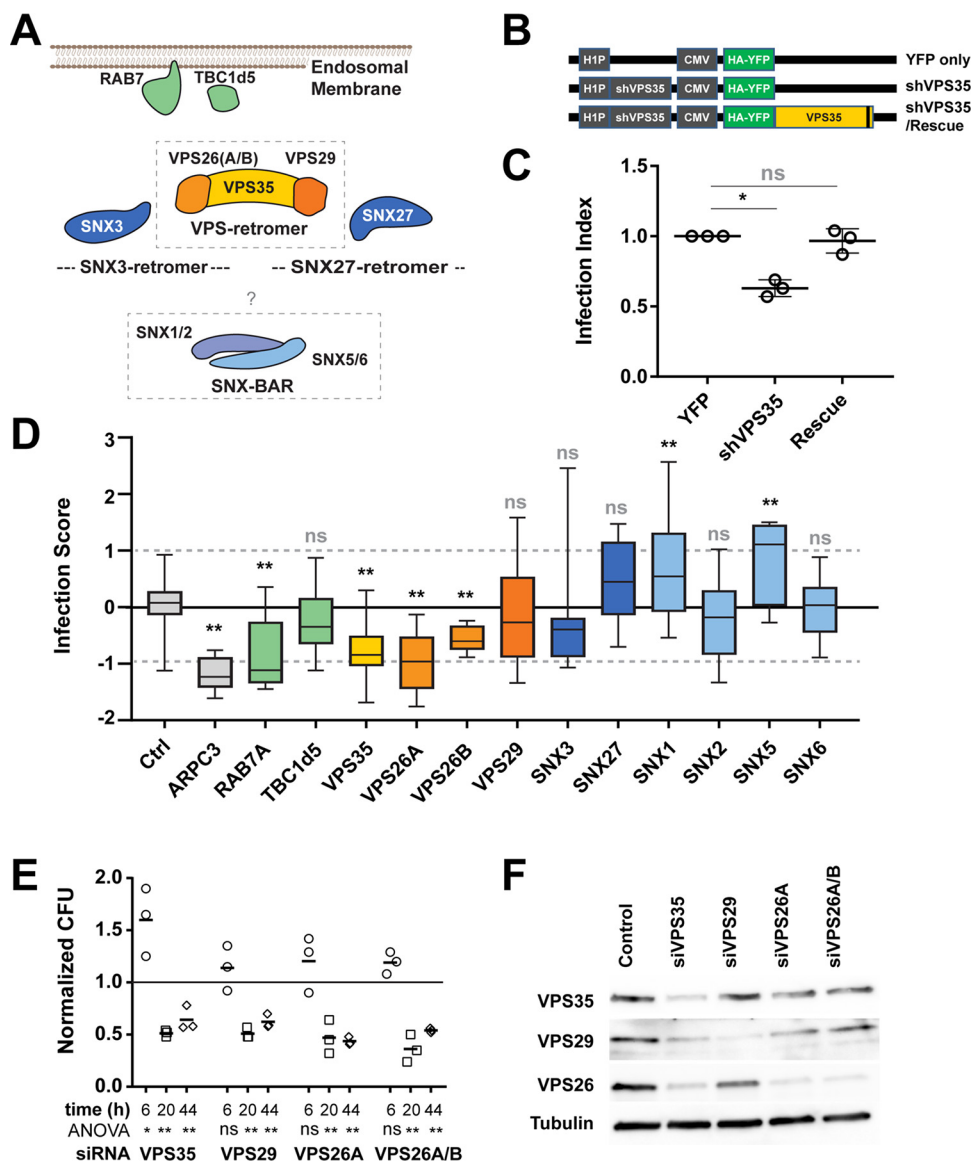
FIG 4 The VPS retromer is a key component of *Brucella* intracellular trafficking. (A) Schematic representation of the retromer components and their prominent interactors. (B) Schematic representation of the shRNA constructs used in panel C. The gray box on the shVPS35/rescue construct indicates the silent mutations that prevent base-pairing with the coexpressed shRNA (41). (C) Infection index from transfected cells. Displayed are the averaged infection index and associated standard deviation after 48 h of *Brucella* infection. Data were normalized to the YFP-only condition ($n = 3$). Values that are statistically significantly different from the value for the scrambled YPF-only condition as determined by paired t test are indicated by an asterisk (*, P value of $\leq$0.01; ns, not significant). (D) Dot box representation of the z-scored infection score for components of the retromer and interactors, including the positive-control ARPC3. Asterisks indicate statistically significant differences from the values for the scrambled siRNA-treated bacteria (control [Ctrl]) as determined by one-way analysis of variance (ANOVA) and Dunnett's multiple-comparison test (**, P value of $\leq$0.001; ns, not significant). (E) Normalized CFU recovered from siRNA-treated cells at 6, 20, or 44 hpi. The presented data correspond to CFU count normalized to control, siRNA-treated cells ($n = 3$). Significance was determined using one-way ANOVA with Dunnett's multiple-comparison test (*, $P \leq$ 0.01; **, $P \leq$ 0.001; ns, not significant). (F) Western blot analysis of the indicated proteins in total lysate of HeLa cells treated with siRNA targeting the designated genes, 72 h posttransfection. Displayed is a representative example of an experiment performed in biological triplicate ($n = 3$). See Table S4 for the matching averaged intensity quantification.

infected HeLa cells at 6 and 18 hpi and determined the percentage of LAMP-1 colocalization for each detected bacteria, combining immunostaining and confocal microscopy (Fig. 5 and Materials and Methods). At 6 hpi, most *Brucella* bacteria were found within LAMP-1-positive vesicles in both control and siRNA-treated cells (Fig. 5A
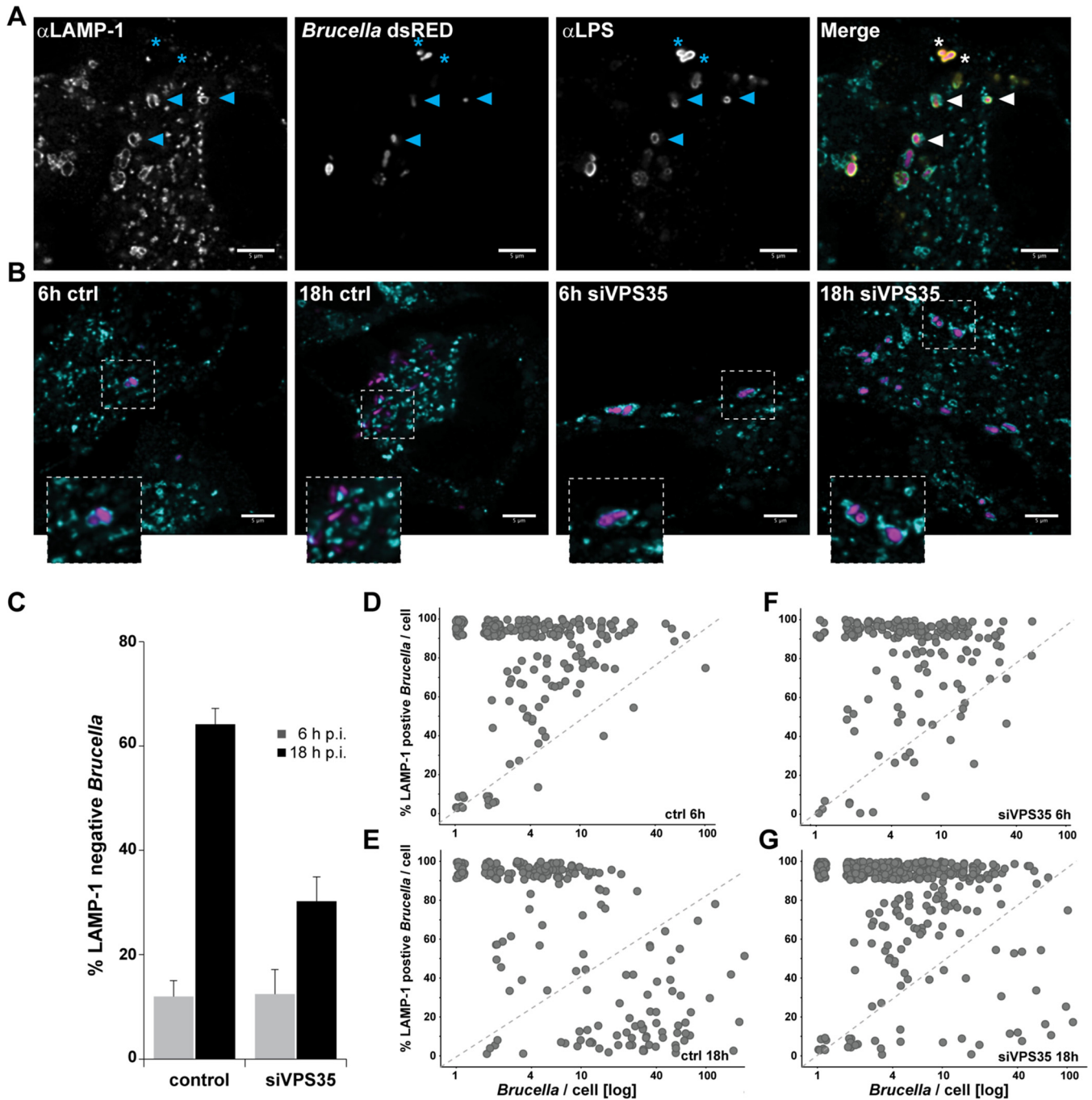
FIG 5 VPS35 is required for *Brucella* to escape the lysosomal pathway. (A) Immunofluorescence approach used to quantify localization of *Brucella* within LAMP-1-positive vesicles, illustrated with a representative example of control-treated cells 6 hpi. Individual channels and merged picture are presented. Arrows indicate examples of colocalization of bacteria with LAMP-1-positive compartments. Staining of *Brucella* LPS (anti-LPS [αLPS]) was used to confirm the presence of LAMP-1 in direct proximity of the bacterial surface. Asterisks indicate examples of LAMP-1-negative *Brucella*. (B) Representative images from *Brucella* infected cells either mock transfected (ctrl) or after VPS35 knockdown (siVPS35). Samples were fixed 6 and 18 hpi. For clarity, only the LAMP-1 (cyan) and dsRed (magenta) channels are presented. Bars, 5 μm. (C) Global quantification of LAMP-1-negative *Brucella*. Displayed are the average and associated standard deviation for more than 500 bacteria and more than 50 HeLa cells per time point and condition (*n* = 3). (D) Single-cell data representation of the data presented in panel C. Displayed is the distribution of LAMP-1-positive *Brucella* per cell as a function of the total number of bacteria counted in that given cell.

to D and F), indicating that VPS35 function is not required for the early trafficking of the BCVs. However, loss of LAMP-1 association at 18 hpi was mainly detected in control cells, whereas most *Brucella* bacteria remained in a LAMP-1-positive compartment upon VPS35 knockdown (Fig. 5B and C). Accordingly, VPS35 depletion strongly reduced intracellular replication of *Brucella* 18 hpi (Fig. 5G) compared to control cells (Fig. 5E).

Altogether, our single-cell colocalization analysis demonstrates the requirement of VPS35, and thus of a functional VPS retromer, for the diversion of BCVs from the lysosomal pathway and for the subsequent establishment of a successful replicative niche.

DISCUSSION

The different membrane-bound organelles that compose the secretory pathway and the endolysosomal system of eukaryotic cells constitute targets of choice for many intracellular pathogens, which have evolved highly diverse strategies to hijack and/or subvert these trafficking pathways to their benefit (2, 3). In that context, the importance of retrograde trafficking for the infection cycle of a number of human pathogens (viruses and bacteria) has been recognized in the past years (e.g., references 42 and 43). This is, for instance, the case for *Chlamydia trachomatis*, which uses its effector LncE to subvert host restriction via direct interaction with SNX5, thereby disrupting retromer trafficking (44, 45). Additional pathogens have been shown to specifically target the VPS retromer, using or subverting its function to their advantage. For instance, hepatitis C virus interacts with VPS35 through its protein NS5A. This viral protein is recognized as VPS retromer cargo, and its interaction with VPS35 supports viral replication (46). Among bacterial pathogens, the best-studied example thus far is the subversion of the VPS retromer function by the T4SS effector RidL of *Legionella pneumophila*. RidL was shown to interact with VPS29, inhibiting retromer activity by outcompeting the binding of the VPS retromer regulator TBC1d5 and thereby promoting *Legionella* intracellular replication (47–49). Most recently, integrity of the *Salmonella*-containing vacuole was shown to be maintained by the direct interaction of the SPI-2 T3SS effector SseC with the VPS retromer (50). In this study, we report the involvement of the VPS retromer in *Brucella* intracellular cycle. More specifically, we show that VPS retromer integrity is required for *Brucella* to escape the host degradative pathway, as supported by the inability of the eBCVs to mature upon VPS35 knockdown toward LAMP-1-negative rBCVs. We further show that this VPS retromer-dependent process takes place after internalization and early trafficking, between 6 h and 18 hpi, matching the estimated timing of the eBCV-to-rBCV transition. It is thus tempting to speculate that the VPS retromer, possibly together with RAB7A, plays a role in this yet elusive but essential branching point of *Brucella* intracellular trafficking, i.e., diversion from the lysosomal pathway toward its ER-associated replicative niche. An alternative, yet nonexclusive hypothesis is that the VPS retromer is involved in the establishment of the rBCV, possibly by providing host factors and/or membranes that follow retrograde trafficking. A further role for the VPS retromer in the maintenance of the rBCV cannot be excluded based on our results. With the accumulation of functional data and the increasing number of described interactors, the VPS retromer is nowadays largely appreciated as a recruiting hub that orchestrates the retrograde endosomal trafficking of numerous cargos to the TGN or the plasma membrane (34, 35, 51). This versatility however obscures the identification of the underlying mechanism(s) by which VPS35 and the VPS retromer may contribute to *Brucella* intracellular fate. Further browsing our data set for the effect of known VPS retromer interactors failed to resolve the VPS retromer-dependent pathway(s)—if any—that is required for *Brucella* intracellular replication. The only VPS retromer interactor that we unambiguously identified is the small GTPase RAB7A, which is essential for the recruitment of the retromer to endosomal membranes (52, 53). Importantly, association of this upstream interactor to the eBCV is a well-established hallmark of early *Brucella* intracellular trafficking (9, 10, 16). Moreover, overexpression of a RAB7 dominant-negative allele (RAB7^{T22N}) impairs the establishment of the *Brucella* replicative niche (10). The importance of RAB7 was recapitulated by our siRNA knockdown approach, strengthening its role in controlling the fate of BCVs, albeit by an unknown mechanism. Considering that the recruitment of the retromer to endosomal membranes is strictly dependent on the presence of RAB7, it is conceivable to assume that depletion of RAB7 prevents the recruitment of VPS35 to the BCV, consequently explaining the RAB7 dependency observed for *Brucella* replication.

Alternatively, very recent findings have established that retromer depletion in HeLa cells actually results in the hyperactivation of RAB7, which causes an overall depletion of the RAB7 pool on endomembranes (54). That drastic consequence could also imply an indirect effect of the observed retromer requirement for *Brucella* trafficking, by acting at the level of RAB7 activity and its availability for the BCV maturation. However, our results indicate that the effects of RAB7A or VPS35 siRNA knockdown are not entirely congruent. Whereas depletion of either factor impairs *Brucella* intracellular replication, only RAB7A knockdown showed a marked effect on pathogen entry, whereas VPS35 appears to be required only at a later stage of the infection. The implications of the newly described feedback signaling on RAB7 triggered by the retromer depletion, as well as the relative contributions of the VPS retromer and RAB7 for the transition of the eBCVs to rBCVs should be addressed in future studies.

Besides the retromer complex, our study pinpointed the involvement of several host pathways in *Brucella* infection, which had not yet been associated with this process. The most prominent cluster negatively affecting infection upon knockdown comprises factors involved in actin remodeling and actin dynamics as well as associated signaling pathways. Apart from an early association of Arp2/3 with BCVs (55), surprisingly little is known about the exact role played by the Arp2/3 complex or the WASP regulatory complex and their regulators during and possibly after *Brucella* internalization. Here as well, further studies will be needed to decipher the precise nature of their involvement. Finally, we also found that members of the TGF-β and fibroblast growth factor (FGF) signaling pathways promote *Brucella* infection, as their depletion decreased the amount of intracellular *Brucella*. Interestingly, it has previously been reported that patients with brucellosis show higher TGF-β1 serum levels, a finding that is correlated with depressed T cell function (56). Further, B cells were also shown to produce TGF-β at early stages of infection with *Brucella* in mice (57). A possible immunosuppressive role for this pathway during *Brucella* infection should be further investigated.

Summing up, we believe that the genes and pathways identified in this study constitute a rich resource toward the understanding of *Brucella* intracellular trafficking, which ultimately should allow development of new approaches to controlling *Brucella* infections in human.

MATERIALS AND METHODS

Cell lines and plasmid constructs. All experiments were performed in the human cervical carcinoma epithelial cell line (HeLa) ATCC CCL-2. Infections were performed using *Brucella abortus* 2308 carrying the constitutive GFP expression plasmid pJC43 (*aphT::GFP*) (58), pAC042.08 for entry assay (*aphT::dsRed tetO::tetR-GFP*) (29), or pAC037 (*aphT::cerulean*) (this study) for rescue experiments. Cells and bacteria were grown as described previously (22, 29). pAC037 was constructed by replacing dsRed from pJC44 (10) with Cerulean from pCERC-1 (59). Cerulean was amplified using prAC082 (TGGATCCGAAAG GAGGTTTATTAAATGGTGAGCAAGGG-CGAGGAGC) and prAC083 (TCTAGAGCTAGCTTACTTGTACAGCTC GTC) and cloned into pJC44 by restriction/ligation using BamHI and XbaI. The ribosomal binding site which was lost on pJC44 using the above restriction was reintroduced on prAC082.

siRNA reverse transfection. Reverse siRNA transfection was performed as described previously (22, 29) with minor adjustments. In brief, genomewide screens were performed with Dharmacon ON-TARGETplus SMART pool (pool of four siRNAs per gene) and Qiagen Human Whole Genome siRNA Set HP GenomeWide (QU, four individual siRNAs for each target). Further validation screens included Ambion Silencer and Ambion Silencer Select custom libraries (with up to six additional siRNAs for about 1,000 genes) and Sigma MISSION esiRNA libraries for 1,900 genes. All screening experiments were conducted in a 384-well plate format. Each plate contained negative controls such as mock (transfection reagent only) and scrambled (nontargeting) siRNA. In addition, general siRNA controls for transfection efficiency and toxicity (e.g., Kif11 [see Fig. S1C in the supplemental material]) as well as positive controls (e.g., Cdc42, Rac1) that are known to have an effect on *Brucella* infection (13) were added to each plate. Based on Kif11, the average transfection efficiency reached 97.6% (91.5 to 99.99%). The following specifications apply to all siRNA screens except the QU siRNA library where specifications are given in brackets. RNAiMAX in Dulbecco modified Eagle medium (DMEM) without fetal calf serum (FCS) was added to each well containing 1.6 pmol siRNA (for QU, 1 pmol) or 15 ng esiRNA. Screening plates were then incubated at room temperature (RT) for 1 h. Following incubation, 500 HeLa cells were seeded per well in DMEM (final concentration of 10% FCS). Plates were incubated at 37°C and 5% CO_2 for 72 h prior to infection. For assays in 96- and 24-well formats, reverse transfections were performed in 6-well plates and subsequently reseeded in the respective plate format. On-target or control siRNAs were added to reach a final siRNA concentration of 20 nM together with RNAiMAX transfection reagent in DMEM without FCS. After 30 min of complex formation at room temperature, 110,000 HeLa cells in DMEM with 10% FCS

(DMEM/10% FCS) were added to each well. After 48 h transfection, cells were harvested by trypsinization and reseeded in DMEM/10% FCS (for 96-well plates, 2,800 cells per well; for 24-well plates, 50,000 cells per well). The next day, cells were infected as described hereafter. The following siRNAs used for CFU determination, colocalization experiments, and/or immunoblotting validation were purchased from Qiagen (Hilden, Germany): VPS35 (SI00760690); VPS26A (SI00760543); VPS26B (SI00631267); VPS29 (SI00760613); all star negative (0001027281); all star death kif11 (0001027299).

Infection. For the genomewide and confirmation screens, infections were performed in 384-well plates as described previously (22, 29). In short, *B. abortus* 2308 pJC43 (*aphT::GFP*) (58) was grown in TSB medium containing 50 μg/ml kanamycin at 37°C to an optical density (OD) of 0.8 to 1.1. Bacteria were then diluted in DMEM/10% FCS and added at a final multiplicity of infection (MOI) of 10,000. Plates were centrifuged at 400 × *g* for 20 min at 4°C to synchronize bacterial entry. After 4 h of incubation at 37°C and 5% CO_2, extracellular bacteria were killed by exchanging the infection medium with DMEM/10% FCS supplemented with 100 μg/ml gentamicin. After a total infection time of 44 h, cells were fixed with 3.7% paraformaldehyde (PFA) for 20 min at RT. For the entry assay, infections were performed as described previously (29). In brief, transfected cells were infected with *B. abortus* 2308 carrying pAC042.08 for 4 h after which GFP expression was induced for 4 h by the addition of anhydrotetracycline (100 ng/ml) during the gentamicin killing of extracellular bacteria. Follow-up experiments and colocalization assays were performed according to the above-described protocol in 96-well and 24-well plates, respectively. For the colocalization assay, cells were infected at an MOI of 2,000. At 2 hpi, cells were washed three times with DMEM/10% FCS containing gentamicin (100 μg/ml). After the indicated incubation time, cells were washed three times with phosphate-buffered saline (PBS) and finally fixed for 20 min in 3.7% PFA (in PBS).

Imaging with high-throughput microscopy. Microscopy was performed with Molecular Devices ImageXpress microscopes. A MetaXpress plate acquisition wizard with no gain, 12-bit dynamic range, and 9 sites per well in a 3 × 3 grid were used with no spacing and no overlap and laser-based focusing. A 4′,6′-diamidino-2-phenylindole (DAPI) channel was used for imaging nuclei, a green fluorescent protein (GFP) channel for bacteria, and a red fluorescent protein (RFP) channel for F-actin or dsRed of bacteria in the entry assay. Robotic plate handling was used to load and unload plates (Thermo Scientific). The objective was a 10× S Fluor with 0.45 numerical aperture (NA). The Site Autofocus was set to "All Sites," and the initial well for finding the sample was set to "First well acquired." Z-Offset for Focus was selected manually, and manual correction of the exposure time was applied to ensure a wide dynamic range with low overexposure. Images from the different siRNA screens are available upon request.

Image analysis. Images were analyzed with the screeningBee analysis framework from BioData-Analysis GmbH. To correct for uneven illumination inherent in wide-field microscopic imaging, an illumination correction model was computed for every plate using Cidre (60). To ensure that the Cidre-corrected image intensities fall within the range [0.0, 1.0], a linear transformation for pixel intensities was computed that maps the 0.001 quantile to 0.01 and the 0.999 quantile to 0.99 postillumination correction. Illumination correction and intensity scaling were performed as preprocessing steps for every image prior to analysis.

To reduce the signal of *Brucella* DNA in the DAPI channel, a linear transform of the GFP channel was subtracted from the DAPI channel, with the linear transformation parameters f and o estimated in the following way: a mapping of GFP pixels to DAPI pixels was constructed so that for all intensities in the GFP images, the list of corresponding intensities in the DAPI images were recorded. For every list of DAPI intensities, only the mean intensities were retained. This creates a mapping of GFP intensities to their corresponding mean DAPI intensities. A linear regression was performed to obtain the linear parameters f and o that map the GFP channel image to the DAPI channel image. Cleaned DAPI images with a reduced *Brucella* signal were obtained by subtracting the linear transform of the GFP channel from the DAPI channel $I'_{DAPI} = I_{DAPI} - (f\,I_{GFP} + o)$ as preprocessing steps for every image prior to analysis. On a random subset of 128 images, CellProfiler (61) was executed to identify nucleus objects using "OTSU Global" segmentation in the DAPI channel, and the median, lower quartile, and upper quartile segmentation thresholds of the images were retained as T_{DAPI-m}, $T_{DAPI-lq}$, and $T_{DAPI-uq}$, respectively. On the same images, the GFP background intensity B_{GFP} was obtained as the position of the peak in the GFP intensity histogram, the dynamic range of the histogram D_{GFP} was obtained as the difference between the 99% quantile and the 1% quantile of intensity values, and the bacterial segmentation threshold was computed as $T_{GFP} = B_{GFP} + \frac{2}{100}D_{GFP}$. On all images, screeningBee CellProfiler was executed to perform object segmentation and measurements with the following steps. (i) Nuclei were detected as primary objects using the manual threshold setting. For each plate, it was manually chosen to use T_{DAPI-m}, $T_{DAPI-lq}$, or $T_{DAPI-uq}$, depending on visual inspection of the segmentation results. Using the same threshold on all images improved site-to-site comparability. (ii) Cells were detected as secondary objects around the nuclei, with "OTSU Global" segmentation in the RFP channel. (iii) Bacteria were detected as primary objects using manual threshold setting with threshold T_{GFP}. Using the fixed background intensity as a reference for T_{GFP} allowed for segmenting even rather dim objects while avoiding site-to-site variability. In order to accurately measure infection scoring, a reliable method to associate pathogen colonies to individual cells is necessary. A straightforward approach is to assume that pathogen colonies must be contained within the body of the host cell. However, high cell confluence can make actin channel-based cell body segmentation inaccurate. Single microcolonies are often split into pieces that are incorrectly assigned to neighboring cells by using this approach (Fig. 1B). To address this issue, we developed a novel algorithm to assign pathogen colonies to robust nucleus objects in an intelligent manner (Fig. 1C).

First, inexpensive "bridge" and "majority" morphological operations were applied to the pathogen objects to connect broken clumps. Next, a weighted distance metric was used to measure an attraction score $a_{N,P}$ between a pathogen P and individual nuclei N within a close proximity (d_{prox}). The attraction score is computed as the surface integral of the nucleus area in a continuous field emanating from the pathogen defined by an exponential function that is strongest within the microcolony itself and that decays exponentially as the distance from the microcolony increases: $a_{N,P} = \sum_{n \in N} e^{-\lambda\, d_{n,P}}$, where n is an element (pixel) belonging to nucleus object N, $d_{n,p}$ is the distance transform from the edge of micro-colony P to n, and λ is a parameter controlling the strength of the decay. Attraction scores for all nuclei proximate to microcolony P are normalized such that the strongest nucleus attraction score is 1,

$\underline{a}_{N,P} = \dfrac{a_{N,P}}{\max(a_{N,P})} \, \forall N$ such that $d_{n,p} < d_{prox}$. Nuclei objects with normalized attraction scores above a threshold a_{min} are associated with the pathogen microcolony. In the case that multiple nuclei are associated with the same microcolony, the microcolony is split so that each element is associated with the nearest nuclei. Large microcolonies are encouraged to split with greater ease than small microcolo-nies by weakening the minimum attraction score linearly according to the area of the microcolony

$a'_{min} = 0.5\, a_{min}$ if $A_P < A_{large}$, or $a'_{min} = 1 - 0.5\, \dfrac{A_P - A_{large}}{A_{large}} a_{min}$ if $A_{large} \leq A_P \leq 2 A_{large}$, and $a'_{min} = 0.5\, a_{min}$ otherwise (where A_P is the area of the pathogen microcolony). Parameters settings $d_{prox} = 45$, $\lambda = 0.2$, $a_{min} = 0.5$, and $A_{large} = 8,000$ were optimized by grid search on a data set of 7,566 hand-labeled segmentations resulting in a 95.58% correct association rate.

Nucleus-to-pathogen microcolony associations were aggregated. The area and integrated intensity of the pathogen objects associated with each cell and the mean intensity of the nuclei in the GFP channel was computed as readout.

Infection scoring for endpoint assays. Wells that contain only 32 cells or less were excluded from infection scoring. In the remaining wells, bacteria were filtered in a decision tree (DT) classification to exclude objects of only one-pixel area. Based on the relation of bacteria to nuclei, for the remaining bacterial objects, the integrated GFP intensity was integrated over all bacteria relating to a cell. To reduce the impact of background intensity, an estimate for GFP background was computed using the 1% lower quantile of mean GFP intensity in the nuclei. For every cell, the estimated GFP background intensity was multiplied with the area of bacteria relating to this cell, and the result was subtracted from the integrated bacterial GFP intensity of the cell to arrive at a background-free estimate of "bacterial load" in each cell. The value range for this intensity was zero for cells with no segmented bacterial objects, and it was higher than zero for all other cells. This integrated GFP intensity was then $\log_2$ scaled, to reflect the exponential growth of replicating *Brucella*. Before $\log_2$ scaling, a small epsilon value of 2^{-20} was added to every cell, so that the $\log_2$ value of cells with no segmented bacteria will not be negative infinity. The arbitrary value 2^{-20} is, by a large margin, smaller than the smallest actual intensity of our assays but large enough to be used in histogram binning. For every plate, the histogram of the $\log_2$-scaled integrated cellular GFP intensity was computed (Fig. 1D) with a bin size of 0.025. The histograms were normalized to an arbitrary "virtual plate cell count" of 10^{10}. To extrapolate a continuous distribution from the possibly sparse histogram, kernel density estimation (KDE) was used with a manually optimized Gaussian kernel of standard deviation 16. The histogram shows a bimodal distribution. By correlating the plate histogram distributions to selected images from the plate, we could identify that the first mode of the distribution is composed of cells with a low number of infection events ranging from single *Brucella* to small clusters, whereas the second mode is composed of large colonies. The two peak positions of the bimodal distribution were identified. Normal distributions G_S and G_L were fitted to the peak positions for small and large colonies, respectively. For the fitting of G_S and G_L, the mean was given by the position of the peak, the height was given by the height of the peak, and the variance was optimized such that the distance between the KDE and the sum of G_S and G_L became minimal. To arrive at a binary infection scoring threshold, we identified a suitable value 3 standard deviations below the mean of G_L. This threshold includes 99.8% of the events in G_L. Cells with an integrated GFP intensity exceeding this threshold were considered true-positive infections and were labeled infected. The infection score was computed as the ratio of infected cells to the total number of cells in the well.

Redundant siRNA analysis and hit selection. Redundant siRNA analysis (RSA) (25) ranks genes by iteratively assigning hypergeometric P values to each of the multiple siRNAs targeting the same gene and picking the minimum value within a given group to represent this gene. The ranking score indicates whether the distribution of ranks corresponding to a gene is shifted toward the top, thereby aggregating the information provided by independent siRNA sequences with the same target in a robust manner. Individual siRNAs from the Qiagen library and the averages of independent replicates of the Dharmacon, Ambion, and Sigma libraries (repeated experiments with identical siRNA) were used as input. Prior to RSA analysis, siRNA targets were reidentified by searching against ENSEMBL cDNA and the REFSEQ mRNA nucleotide data in order to ensure comparability between libraries. Cases where matching failed were excluded from this analysis. Data were further filtered by removing all wells that do not pass quality control, control wells and wells where cell count was below the initially seeded cell number (500). As both up-hits and down-hits are of interest to this analysis, RSA was run twice, once with Z-scored infection scores ranked from low to high values and once ranked oppositely. The RSA parameters were set as follows: upper and lower bound (-0.5; -2) or (-0.5; -10) on averaged z-scored infection score for down- and up-hits, respectively. Bonferroni correction was applied to account for the different numbers of siRNAs per gene. Genes matching a Benjamini-corrected RSA P value of ≤ 0.01 with more than three hit wells were considered significant and selected for further analysis.

Infection scoring for entry assays. Wells containing only 32 cells or less were excluded from infection scoring. In the remaining wells, bacteria were filtered in a decision tree (DT) classification to exclude objects of only one pixel area. The remaining bacteria were filtered in a DT classification to exclude objects of less than a manually set threshold on the upper quartile of the object intensity. The remaining bacteria were considered true-positive infections. Based on the relation of bacteria to nuclei, cells were labeled infected if and only if a true-positive bacteria is related to the cell's nuclei. The infection score was computed as the ratio of infected cells to the total number of cells in the well. For quantification of bacterial load in infected cells, the median of integrated GFP intensity of all true-positive bacteria was computed. The final infection readout was the product of the infection rate and bacterial load, which gives a robust approximation of the amount of intracellular bacteria (29).

Rescue experiment. The shRNA suppression/rescue constructs for VPS35 were kind gifts from Daniel Billadeau (41). HeLa cells were seeded in a six-well plate and transfected 4 h later with 0.9 μg of plasmid DNA using Fugene HD according to the manufacturer's protocol. At 72 h posttransfection, cells were reseeded into a 96-well plate (2,800 cells/well) and infected on the following day. Cells were infected with *Brucella abortus* carrying pAC037 for 48 h. After PFA fixation and staining, cells were analyzed by image analysis. Infection scoring was performed on yellow fluorescent protein (YFP)-positive cells, indicative of successful transfection.

Determination of intracellular bacterial load by CFU determination. Infections of siRNA-transfected HeLa cells were performed in 96-well plates as described above. At 6, 20, or 44 hpi, infected cells were washed with 200 μl PBS and lysed for 10 min with 0.1% Triton X-100/PBS. Lysed cells (six wells per conditions) were collected in 2-ml screw-cap tubes and washed once with 1 ml PBS. The pellet was resuspended in 1 ml PBS and subjected to fivefold serial dilution before plating onto TSA plate. CFU were counted after 3 days growth at 37°C and normalized to the CFU obtained by the scrambled siRNA-treated cells from the matching biological replicate.

Immunoblotting. Proteins from total cell lysates (10 to 20 μg) were separated by SDS-PAGE, transferred onto PVDF membranes (Hybond 0.2 μm; Amersham GE Life Sciences), and probed using the indicated antibodies. The secondary HRP-conjugated antibody was visualized by chemiluminescence (SeraCare developer solution). For anti-tubulin probing, membranes were first treated with stripping buffer (Thermo Scientific), washed, and reprobed. Polyclonal rabbit antibodies against VPS35 (ab97545; abcam), VPS29 (ab98929; abcam), rabbit monoclonal antibody against VPS26 (ab98929; abcam) or mouse monoclonal antibody against β-tubulin (catalog no. T8328; Sigma) were used according to the manufacturer's instructions. Quantification of immunoblots was performed using ImageJ.

Immunofluorescence for LAMP-1 colocalization. Following fixation with 3.7% PFA in PBS for 20 min, HeLa cells were incubated in PBS containing 250 mM glycine for 20 min to quench remaining aldehyde residues. Cells were then permeabilized with saponin buffer (PBS containing 0.2% saponin and 3% bovine serum albumin) for 1 h. Immunostaining was performed by incubating coverslips with saponin buffer containing antibodies against LAMP-1 (ab25630; abcam) and *Brucella abortus* lipopolysaccharide (LPS) polyclonal rabbit serum (kind gift from Xavier De Bolle [62]) overnight in a humidified chamber at 4°C. The coverslips were then washed three times with PBS and incubated with saponin buffer containing respective fluorophore-conjugated secondary antibodies: goat anti-mouse Alexa Fluor 488 (catalog no. A11029; Thermo Fisher) and anti-rabbit Alexa Fluor 647 (catalog no. 4414; Cell Signaling) for 3 h in a humidified chamber at room temperature. The coverslips were then washed three times with PBS and mounted onto glass slides using Vectashield H-100 antifade mounting medium (Vector Laboratories) and sealed with nail polish.

Confocal microscopy for single-cell data. The images were captured with the LSM-800 confocal microscope (Carl Zeiss) using a 63× oil objective. For each condition, 40 images were obtained at random locations across the coverslip, representing more than 50 individual cells per conditions. The images were deconvolved using Huygens software (Scientific Volume Imaging). The presence of LAMP-1 signal around the bacteria was quantified from the images by assessing the overlap between the anti-LPS and the anti-LAMP-1 staining for each individual bacterium (more than 400 per condition).

SUPPLEMENTAL MATERIAL

Supplemental material for this article may be found at https://doi.org/10.1128/mSphere.00380-19.

FIG S1, TIF file, 2.1 MB.
FIG S2, EPS file, 2.5 MB.
FIG S3, EPS file, 2.8 MB.
TABLE S1, XLSX file, 0.02 MB.
TABLE S2, XLSX file, 0.02 MB.
TABLE S3, XLSX file, 0.2 MB.
TABLE S4, PDF file, 0.02 MB.

ACKNOWLEDGMENTS

REFERENCES

1. Creasey EA, Isberg RR. 2014. Maintenance of vacuole integrity by bacterial pathogens. Curr Opin Microbiol 17:46–52. https://doi.org/10.1016/j.mib.2013.11.005.

2. Di Russo Case E, Samuel JE. 2016. Contrasting lifestyles within the host cell. Microbiol Spectr 4(1):VMBF-0014-2015. https://doi.org/10.1128/microbiolspec.VMBF-0014-2015.

3. Weber MM, Faris R. 2018. Subversion of the endocytic and secretory pathways by bacterial effector proteins. Front Cell Dev Biol 6:1. https://doi.org/10.3389/fcell.2018.00001.

4. Havelaar AH, Kirk MD, Torgerson PR, Gibb HJ, Hald T, Lake RJ, Praet N, Bellinger DC, de Silva NR, Gargouri N, Speybroeck N, Cawthorne A, Mathers C, Stein C, Angulo FJ, Devleesschauwer B, World Health Organization Foodborne Disease Burden Epidemiology Reference Group. 2015. World Health Organization global estimates and regional comparisons of the burden of foodborne disease in 2010. PLoS Med 12: e1001923. https://doi.org/10.1371/journal.pmed.1001923.

5. Moreno E. 2014. Retrospective and prospective perspectives on zoonotic brucellosis. Front Microbiol 5:213. https://doi.org/10.3389/fmicb.2014.00213.

6. Pappas G, Papadimitriou P, Akritidis N, Christou L, Tsianos EV. 2006. The new global map of human brucellosis. Lancet Infect Dis 6:91–99. https://doi.org/10.1016/S1473-3099(06)70382-6.

7. Ariza J, Bosilkovski M, Cascio A, Colmenero JD, Corbel MJ, Falagas ME, Memish ZA, Roushan MR, Rubinstein E, Sipsas NV, Solera J, Young EJ, Pappas G, International Society of Chemotherapy, Institute of Continuing Medical Education of Ioannina. 2007. Perspectives for the treatment of brucellosis in the 21st century: the Ioannina recommendations. PLoS Med 4:e317. https://doi.org/10.1371/journal.pmed.0040317.

8. Sedzicki J, Tschon T, Low SH, Willemart K, Goldie KN, Letesson JJ, Stahlberg H, Dehio C. 2018. 3D correlative electron microscopy reveals continuity of *Brucella*-containing vacuoles with the endoplasmic reticulum. J Cell Sci 131:jcs210799. https://doi.org/10.1242/jcs.210799.

9. Pizarro-Cerdá J, Méresse S, Parton RG, van der Goot G, Sola-Landa A, Lopez-Goñi I, Moreno E, Gorvel JP. 1998. *Brucella abortus* transits through the autophagic pathway and replicates in the endoplasmic reticulum of nonprofessional phagocytes. Infect Immun 66:5711–5724.

10. Starr T, Ng TW, Wehrly TD, Knodler LA, Celli J. 2008. *Brucella* intracellular replication requires trafficking through the late endosomal/lysosomal compartment. Traffic 9:678–694. https://doi.org/10.1111/j.1600-0854.2008.00718.x.

11. Castañeda-Roldán EI, Avelino-Flores F, Dall'Agnol M, Freer E, Cedillo L, Dornand J, Girón JA. 2004. Adherence of *Brucella* to human epithelial cells and macrophages is mediated by sialic acid residues. Cell Microbiol 6:435–445. https://doi.org/10.1111/j.1462-5822.2004.00372.x.

12. Castañeda-Roldán EI, Ouahrani-Bettache S, Saldaña Z, Avelino F, Rendón MA, Dornand J, Girón JA. 2006. Characterization of SP41, a surface protein of *Brucella* associated with adherence and invasion of host epithelial cells. Cell Microbiol 8:1877–1887. https://doi.org/10.1111/j.1462-5822.2006.00754.x.

13. Guzmán-Verri C, Chaves-Olarte E, von Eichel-Streiber C, López-Goñi I, Thelestam M, Arvidson S, Gorvel JP, Moreno E. 2001. GTPases of the Rho subfamily are required for *Brucella abortus* internalization in nonprofessional phagocytes: direct activation of Cdc42. J Biol Chem 276: 44435–44443. https://doi.org/10.1074/jbc.M105606200.

14. Arellano-Reynoso B, Lapaque N, Salcedo S, Briones G, Ciocchini AE, Ugalde R, Moreno E, Moriyón I, Gorvel J-P. 2005. Cyclic beta-1,2-glucan is a *Brucella* virulence factor required for intracellular survival. Nat Immunol 6:618–625. https://doi.org/10.1038/ni1202.

15. Bellaire BH, Roop RM, Jr, Cardelli JA. 2005. Opsonized virulent *Brucella abortus* replicates within nonacidic, endoplasmic reticulum-negative,

LAMP-1-positive phagosomes in human monocytes. Infect Immun 73: 3702–3713. https://doi.org/10.1128/IAI.73.6.3702-3713.2005.

16. Celli J, de Chastellier C, Franchini DM, Pizarro-Cerda J, Moreno E, Gorvel JP. 2003. *Brucella* evades macrophage killing via VirB-dependent sustained interactions with the endoplasmic reticulum. J Exp Med 198: 545–556. https://doi.org/10.1084/jem.20030088.

17. Boschiroli ML, Ouahrani-Bettache S, Foulongne V, Michaux-Charachon S, Bourg G, Allardet-Servent A, Cazevieille C, Liautard JP, Ramuz M, O'Callaghan D. 2002. The *Brucella suis virB* operon is induced intracellularly in macrophages. Proc Natl Acad Sci U S A 99:1544–1549. https://doi.org/10.1073/pnas.032514299.

18. Comerci DJ, Martinez-Lorenzo MJ, Sieira R, Gorvel JP, Ugalde RA. 2001. Essential role of the VirB machinery in the maturation of the *Brucella abortus*-containing vacuole. Cell Microbiol 3:159–168. https://doi.org/10.1046/j.1462-5822.2001.00102.x.

19. Ke Y, Wang Y, Li W, Chen Z. 2015. Type IV secretion system of *Brucella* spp. and its effectors. Front Cell Infect Microbiol 5:72. https://doi.org/10.3389/fcimb.2015.00072.

20. Miller CN, Smith EP, Cundiff JA, Knodler LA, Bailey Blackburn J, Lupashin V, Celli J. 2017. A *Brucella* type IV effector targets the COG tethering complex to remodel host secretory traffic and promote intracellular replication. Cell Host Microbe 22:317–329.e7. https://doi.org/10.1016/j.chom.2017.07.017.

21. Franceschini A, Meier R, Casanova A, Kreibich S, Daga N, Andritschke D, Dilling S, Ramo P, Emmenlauer M, Kaufmann A, Conde-Alvarez R, Low SH, Pelkmans L, Helenius A, Hardt WD, Dehio C, von Mering C. 2014. Specific inhibition of diverse pathogens in human cells by synthetic microRNA-like oligonucleotides inferred from RNAi screens. Proc Natl Acad Sci U S A 111:4548–4553. https://doi.org/10.1073/pnas.1402353111.

22. Rämö P, Drewek A, Arrieumerlou C, Beerenwinkel N, Ben-Tekaya H, Cardel B, Casanova A, Conde-Alvarez R, Cossart P, Csúcs G, Eicher S, Emmenlauer M, Greber U, Hardt W-D, Helenius A, Kasper C, Kaufmann A, Kreibich S, Kühbacher A, Kunszt P, Low SH, Mercer J, Mudrak D, Muntwiler S, Pelkmans L, Pizarro-Cerdá J, Podvinec M, Pujadas E, Rinn B, Rouilly V, Schmich F, Siebourg-Polster J, Snijder B, Stebler M, Studer G, Szczurek E, Truttmann M, von Mering C, Vonderheit A, Yakimovich A, Bühlmann P, Dehio C. 2014. Simultaneous analysis of large-scale RNAi screens for pathogen entry. BMC Genomics 15:1162. https://doi.org/10.1186/1471-2164-15-1162.

23. Québatte M, Dehio C. 2017. Systems-level interference strategies to decipher host factors involved in bacterial pathogen interaction: from RNAi to CRISPRi. Curr Opin Microbiol 39:34–41. https://doi.org/10.1016/j.mib.2017.08.002.

24. Zhu J, Davoli T, Perriera JM, Chin CR, Gaiha GD, John SP, Sigiollot FD, Gao G, Xu Q, Qu H, Pertel T, Sims JS, Smith JA, Baker RE, Maranda L, Ng A, Elledge SJ, Brass AL. 2014. Comprehensive identification of host modulators of HIV-1 replication using multiple orthologous RNAi reagents. Cell Rep 9:752–766. https://doi.org/10.1016/j.celrep.2014.09.031.

25. Konig R, Chiang CY, Tu BP, Yan SF, DeJesus PD, Romero A, Bergauer T, Orth A, Krueger U, Zhou Y, Chanda SK. 2007. A probability-based approach for the analysis of large-scale RNAi screens. Nat Methods 4:847–849. https://doi.org/10.1038/nmeth1089.

26. Huang DW, Sherman BT, Lempicki RA. 2009. Systematic and integrative analysis of large gene lists using DAVID bioinformatics resources. Nat Protoc 4:44–57. https://doi.org/10.1038/nprot.2008.211.

27. Szklarczyk D, Morris JH, Cook H, Kuhn M, Wyder S, Simonovic M, Santos A, Doncheva NT, Roth A, Bork P, Jensen LJ, von Mering C. 2017. The STRING database in 2017: quality-controlled protein-protein association networks, made broadly accessible. Nucleic Acids Res 45:D362–D368. https://doi.org/10.1093/nar/gkw937.

28. Keriel A, Botella E, Estrach S, Bragagnolo G, Vergunst AC, Feral CC, O'Callaghan D. 2015. *Brucella* intracellular life relies on the transmembrane protein CD98 heavy chain. J Infect Dis 211:1769–1778. https://doi.org/10.1093/infdis/jiu673.

29. Casanova A, Low SH, Emmenlauer M, Conde-Alvarez R, Salcedo SP, Gorvel JP, Dehio C. 2016. Microscopy-based assays for high-throughput screening of host factors involved in *Brucella* infection of Hela cells. J Vis Exp https://doi.org/10.3791/54263.

30. Morth JP, Pedersen BP, Buch-Pedersen MJ, Andersen JP, Vilsen B, Palmgren MG, Nissen P. 2011. A structural overview of the plasma membrane Na+, K+-ATPase and H+-ATPase ion pumps. Nat Rev Mol Cell Biol 12:60–70. https://doi.org/10.1038/nrm3031.

31. Siezen RJ, Leunissen JA. 1997. Subtilases: the superfamily of subtilisin-like serine proteases. Protein Sci 6:501–523. https://doi.org/10.1002/pro.5560060301.

32. Linxweiler M, Schick B, Zimmermann R. 2017. Let's talk about Secs: Sec61, Sec62 and Sec63 in signal transduction, oncology and personalized medicine. Signal Transduct Target Ther 2:17002. https://doi.org/10.1038/sigtrans.2017.2.

33. Qin QM, Pei J, Ancona V, Shaw BD, Ficht TA, de Figueiredo P. 2008. RNAi screen of endoplasmic reticulum-associated host factors reveals a role for IRE1alpha in supporting *Brucella* replication. PLoS Pathog 4:e1000110. https://doi.org/10.1371/journal.ppat.1000110.

34. Gallon M, Cullen PJ. 2015. Retromer and sorting nexins in endosomal sorting. Biochem Soc Trans 43:33–47. https://doi.org/10.1042/BST20140290.

35. Wang J, Fedoseienko A, Chen B, Burstein E, Jia D, Billadeau DD. 2018. Endosomal receptor trafficking: Retromer and beyond. Traffic 19: 578–590. https://doi.org/10.1111/tra.12574.

36. Steinberg F, Gallon M, Winfield M, Thomas EC, Bell AJ, Heesom KJ, Tavare JM, Cullen PJ. 2013. A global analysis of SNX27-retromer assembly and cargo specificity reveals a function in glucose and metal ion transport. Nat Cell Biol 15:461–471. https://doi.org/10.1038/ncb2721.

37. Temkin P, Lauffer B, Jager S, Cimermancic P, Krogan NJ, von Zastrow M. 2011. SNX27 mediates retromer tubule entry and endosome-to-plasma membrane trafficking of signalling receptors. Nat Cell Biol 13:715–721. https://doi.org/10.1038/ncb2252.

38. Seaman MN, McCaffery JM, Emr SD. 1998. A membrane coat complex essential for endosome-to-Golgi retrograde transport in yeast. J Cell Biol 142:665–681. https://doi.org/10.1083/jcb.142.3.665.

39. Kvainickas A, Jimenez-Orgaz A, Nagele H, Hu Z, Dengjel J, Steinberg F. 2017. Cargo-selective SNX-BAR proteins mediate retromer trimer independent retrograde transport. J Cell Biol 216:3677–3693. https://doi.org/10.1083/jcb.201702137.

40. Simonetti B, Danson CM, Heesom KJ, Cullen PJ. 2017. Sequence-dependent cargo recognition by SNX-BARs mediates retromer-independent transport of CI-MPR. J Cell Biol 216:3695–3712. https://doi.org/10.1083/jcb.201703015.

41. Liu TT, Gomez TS, Sackey BK, Billadeau DD, Burd CG. 2012. Rab GTPase regulation of retromer-mediated cargo export during endosome maturation. Mol Biol Cell 23:2505–2515. https://doi.org/10.1091/mbc.E11-11-0915.

42. Elwell C, Engel J. 2018. Emerging role of retromer in modulating pathogen growth. Trends Microbiol 26:769–780. https://doi.org/10.1016/j.tim.2018.04.001.

43. Personnic N, Barlocher K, Finsel I, Hilbi H. 2016. Subversion of retrograde trafficking by translocated pathogen effectors. Trends Microbiol 24: 450–462. https://doi.org/10.1016/j.tim.2016.02.003.

44. Elwell CA, Czudnochowski N, von Dollen J, Johnson JR, Nakagawa R, Mirrashidi K, Krogan NJ, Engel JN, Rosenberg OS. 2017. *Chlamydia* interfere with an interaction between the mannose-6-phosphate receptor and sorting nexins to counteract host restriction. Elife 6:e22709. https://doi.org/10.7554/eLife.22709.

45. Mirrashidi KM, Elwell CA, Verschueren E, Johnson JR, Frando A, Von Dollen J, Rosenberg O, Gulbahce N, Jang G, Johnson T, Jager S, Gopalakrishnan AM, Sherry J, Dunn JD, Olive A, Penn B, Shales M, Cox JS, Starnbach MN, Derre I, Valdivia R, Krogan NJ, Engel J. 2015. Global mapping of the Inc-human interactome reveals that retromer restricts chlamydia infection. Cell Host Microbe 18:109–121. https://doi.org/10.1016/j.chom.2015.06.004.

46. Yin P, Hong Z, Yang X, Chung RT, Zhang L. 2016. A role for retromer in hepatitis C virus replication. Cell Mol Life Sci 73:869–881. https://doi.org/10.1007/s00018-015-2027-7.

47. Yao J, Yang F, Sun X, Wang S, Gan N, Liu Q, Liu D, Zhang X, Niu D, Wei Y, Ma C, Luo ZQ, Sun Q, Jia D. 2018. Mechanism of inhibition of retromer transport by the bacterial effector RidL. Proc Natl Acad Sci U S A 115:E1446–E1454. https://doi.org/10.1073/pnas.1717383115.

48. Romano-Moreno M, Rojas AL, Williamson CD, Gershlick DC, Lucas M, Isupov MN, Bonifacino JS, Machner MP, Hierro A. 2017. Molecular mechanism for the subversion of the retromer coat by the *Legionella* effector RidL. Proc Natl Acad Sci U S A 114:E11151–E11160. https://doi.org/10.1073/pnas.1715361115.

49. Barlocher K, Hutter CAJ, Swart AL, Steiner B, Welin A, Hohl M, Letourneur F, Seeger MA, Hilbi H. 2017. Structural insights into *Legionella* RidL-Vps29 retromer subunit interaction reveal displacement of the regulator TBC1D5. Nat Commun 8:1543. https://doi.org/10.1038/s41467-017-01512-5.

50. Patrick KL, Wojcechowskyj JA, Bell SL, Riba MN, Jing T, Talmage S, Xu P, Cabello AL, Xu J, Shales M, Jimenez-Morales D, Ficht TA, de Figueiredo P, Samuel JE, Li P, Krogan NJ, Watson RO. 2018. Quantitative yeast genetic interaction profiling of bacterial effector proteins uncovers a role for the human retromer in *Salmonella* infection. Cell Syst 7:323–338.e6. https://doi.org/10.1016/j.cels.2018.06.010.

51. Harbour ME, Breusegem SY, Antrobus R, Freeman C, Reid E, Seaman MN. 2010. The cargo-selective retromer complex is a recruiting hub for protein complexes that regulate endosomal tubule dynamics. J Cell Sci 123:3703–3717. https://doi.org/10.1242/jcs.071472.

52. Harrison MS, Hung CS, Liu TT, Christiano R, Walther TC, Burd CG. 2014. A mechanism for retromer endosomal coat complex assembly with cargo. Proc Natl Acad Sci U S A 111:267–272. https://doi.org/10.1073/pnas.1316482111.

53. Seaman MN, Harbour ME, Tattersall D, Read E, Bright N. 2009. Membrane recruitment of the cargo-selective retromer subcomplex is catalysed by the small GTPase Rab7 and inhibited by the Rab-GAP TBC1D5. J Cell Sci 122:2371–2382. https://doi.org/10.1242/jcs.048686.

54. Jimenez-Orgaz A, Kvainickas A, Nagele H, Denner J, Eimer S, Dengjel J, Steinberg F. 2018. Control of RAB7 activity and localization through the retromer-TBC1D5 complex enables RAB7-dependent mitophagy. EMBO J 37:235–254. https://doi.org/10.15252/embj.201797128.

55. Lee JJ, Kim DG, Kim DH, Simborio HL, Min W, Lee HJ, Her M, Jung SC, Watarai M, Kim S. 2013. Interplay between clathrin and Rab5 controls the early phagocytic trafficking and intracellular survival of *Brucella abortus* within HeLa cells. J Biol Chem 288:28049–28057. https://doi.org/10.1074/jbc.M113.491555.

56. Elfaki MG, Al-Hokail AA. 2009. Transforming growth factor beta production correlates with depressed lymphocytes function in humans with chronic brucellosis. Microbes Infect 11:1089–1096. https://doi.org/10.1016/j.micinf.2009.08.001.

57. Goenka R, Parent MA, Elzer PH, Baldwin CL. 2011. B cell-deficient mice display markedly enhanced resistance to the intracellular bacterium *Brucella abortus*. J Infect Dis 203:1136–1146. https://doi.org/10.1093/infdis/jiq171.

58. Celli J, Salcedo SP, Gorvel JP. 2005. *Brucella* coopts the small GTPase Sar1 for intracellular replication. Proc Natl Acad Sci U S A 102:1673–1678. https://doi.org/10.1073/pnas.0406873102.

59. Thanbichler M, Iniesta AA, Shapiro L. 2007. A comprehensive set of plasmids for vanillate- and xylose-inducible gene expression in *Caulobacter crescentus*. Nucleic Acids Res 35:e137. https://doi.org/10.1093/nar/gkm818.

60. Smith K, Li Y, Piccinini F, Csucs G, Balazs C, Bevilacqua A, Horvath P. 2015. CIDRE: an illumination-correction method for optical microscopy. Nat Methods 12:404–406. https://doi.org/10.1038/nmeth.3323.

61. Carpenter AE, Jones TR, Lamprecht MR, Clarke C, Kang IH, Friman O, Guertin DA, Chang JH, Lindquist RA, Moffat J, Golland P, Sabatini DM. 2006. CellProfiler: image analysis software for identifying and quantifying cell phenotypes. Genome Biol 7:R100. https://doi.org/10.1186/gb-2006-7-10-r100.

62. Deghelt M, Mullier C, Sternon JF, Francis N, Laloux G, Dotreppe D, Van der Henst C, Jacobs-Wagner C, Letesson JJ, De Bolle X. 2014. G1-arrested newborn cells are the predominant infectious form of the pathogen *Brucella abortus*. Nat Commun 5:4366. https://doi.org/10.1038/ncomms5366.

63. Keleher LL, Skyberg JA. 2016. Activation of bovine neutrophils by *Brucella* spp. Vet Immunol Immunopathol 177:1–6. https://doi.org/10.1016/j.vetimm.2016.05.011.

64. Starr T, Child R, Wehrly TD, Hansen B, Hwang S, Lopez-Otin C, Virgin HW, Celli J. 2012. Selective subversion of autophagy complexes facilitates completion of the *Brucella* intracellular cycle. Cell Host Microbe 11:33–45. https://doi.org/10.1016/j.chom.2011.12.002.